

Theoretical and Experimental Investigation of the Fast- and Slow-Scale Instabilities of a DC–DC Converter

Sudip K. Mazumder, Ali H. Nayfeh, and Dushan Boroyevich, *Member, IEEE*

Abstract—We use an exact formulation based on nonlinear maps to investigate both the fast-scale and slow-scale instabilities of a voltage-mode buck converter operating in the continuous conduction mode and its interaction with a filter. Comparing the results of the exact model with those of the averaged model shows the shortcomings of the latter in predicting fast-scale instabilities. We show the impact of parasitics on the onset of chaos using a high-frequency model. The experimentally validated theoretical results of this paper provide an improved understanding of the dynamics of the converter beyond the linear regime and this may lead to less conservative control design and newer applications.

Index Terms—Bifurcation, converters, differential inclusion, discontinuous systems.

I. INTRODUCTION

POWER ELECTRONIC converters are nonlinear dynamical systems. The nonlinearities arise primarily due to switching, power devices, and passive components, such as transformers, inductors, and parasitics. Historically, there have been four major approaches to the modeling and analysis of the switching nonlinearity in dc–dc converters. The most widely used approach is a small-signal analysis based on state-space averaging or circuit averaging using the pulse-width modulation (PWM) switch model [1]–[4]. This approach fails to predict the fast-scale dynamics and can capture only the slow-scale dynamics. The second approach is based on the sampled-data modeling technique [5]–[8]. It is an improvement over the averaged modeling technique. It takes into account the sampling effect due to switching and can predict the boundary of the period-one instability. It is currently, however, limited to current-mode converters and is difficult to use for analyzing chaotic dynamics. The third approach describes the switched-mode power supply using a typical continuous time model of the form $\dot{\psi} = f(\psi, u, t)$, where the right-hand side is discontinuous due to abrupt changes in the control u . This class of models is one of the hardest to study [9]–[13]. Besides,

the existence of solutions for this class of systems is not always well-defined. On the other hand, a discrete-time formulation of the switched-mode operation does not involve discontinuities due to control action and results in smooth functions that describe the system. The last approach, which is known as the discrete modeling technique, was first used by Prajoux *et al.* [14] for power converter modeling. Later, it was used by Wood [15] and Deane and Hamill [16] to investigate the regions of the fast-scale instability in buck converters operating in the continuous-conduction mode (CCM). Since then some exciting results have been published, which extend this investigation to a few other dc–dc converters operating in the CCM and the discontinuous conduction mode (DCM) [17]–[26].

Most of the earlier work in this field dealt with idealized circuits and demonstrated some of the nonlinear phenomenon in such bare-bone systems. In this paper, we treat the converter as a power-electronic system and not just as a circuit. Using an exact formulation based on nonlinear maps [14]–[16], we develop a systematic method to model dc–dc converters operating with static or dynamic feedback control. We use this methodology to investigate the fast-scale instabilities of a high-frequency voltage-mode buck converter that employs dynamic-feedback control for voltage regulation and operates in the CCM. The basic idea can, however, be easily extended to other classes of dc–dc converters, including parallel dc–dc converters [26], and even single-phase power-factor-correction circuits [13]. We validate experimentally the theoretical results for the voltage-mode buck converter. We also extend this analysis to an integrated system involving a voltage-mode buck converter and a second-order input filter at its front end. For both cases, we compare the results obtained with the exact formulation with those obtained using state-space averaged models and point out the shortcoming of averaged models in predicting fast-scale instabilities in systems that are closer to converters used in practice. Hamill [27], pointed out the shortcomings of averaged models in predicting fast-scale instabilities in an idealized circuit representing a buck converter. The approach in this paper is systematic and can be used to investigate slow- and fast-scale instabilities in any other class of dc–dc converters [26]. It can also be applied to systems with static- or dynamic-feedback control, or multiloop control with minimal changes. For example, in [26], we have extended the methodology to parallel dc–dc converters. Unlike [27], the analysis in this paper includes the effect of the parasitics in the nominal model and extends the methodology to analyze the stability of an integrated converter.

Manuscript received January 7, 2000; revised December 13, 2000. This work was supported by the Office of Naval Research under Grant N00014-96-1-1123 and made use of ERC Shared Facilities supported by the National Science Foundation under Award EEC-9731677. Recommended by Associate Editor C. K. Tse.

S. K. Mazumder and D. Boroyevich are with the Center for Power Electronics Systems, Department of Electrical and Computer Engineering, Virginia Polytechnic Institute and State University, Blacksburg, VA 24061 USA.

A. H. Nayfeh is with the Department of Engineering Science and Mechanics, Virginia Polytechnic Institute and State University, Blacksburg, VA 24061 USA.
Publisher Item Identifier S 0885-8993(01)02190-1.

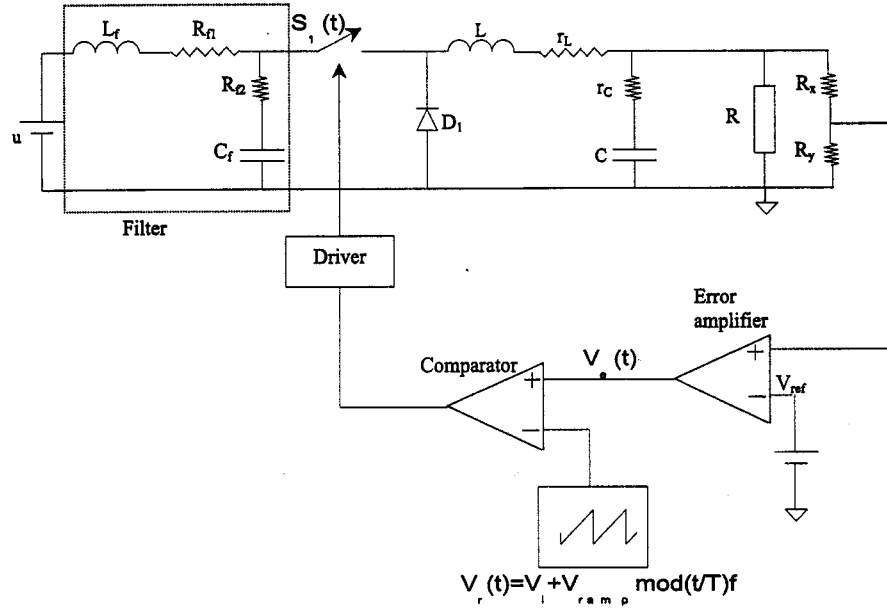


Fig. 1. Closed-loop buck converter with a second-order filter at its front end.

Currently, most of the commercial dc–dc converters operate at 100 kHz or above. At such high frequencies the effects of parasitic elements can not be ignored as has been done in the past by most investigators. Therefore, in this paper we also demonstrate the impact of very high-frequency dynamics, due to parasitics and device nonlinearities, on the onset of chaos by developing a high-frequency model. The parasitic parameters for this model are obtained using a finite-element analysis package based on the actual printed-circuit board (PCB) of the experimental converter.

The analyses in this paper are based on systems that are close to dc–dc converters used in practice and hence, the results should be of interest to practicing engineers. The present results indicate that nonlinear analyzes of power converters lead to a better understanding of their dynamics. With these analyzes, one can clearly demarcate the boundaries of instabilities (without resorting to time consuming numerical simulations) and demonstrate the fast-scale and slow-scale instabilities. This may lead to converters that have better design and performance.

II. MODELING AND ANALYSIS

Initially, we assume that the nonlinearities due to the power device and parasitics are negligible. Then, we demonstrate their effect through a high-frequency model. The converter is clocked at a rate equal to the switching frequency. Moreover, the controller is designed in such a way that, once a change of state is latched, it can be reset only by the next clock. This effectively eliminates the possibility of multiple pulses. We analyze the closed-loop buck converter (without the filter) first and then extend the analysis to the integrated system.

The buck converter operating under the CCM and duty-ratio control is a piecewise-smooth system. The multitopological system, shown in Fig. 1, is in the on-state (for duration T_1)

when S_1 is closed and in the off-state (for duration T_2) when S_1 is open. If we represent the two states, the inductor current $[i_L(t)]$ and the output capacitor voltage $[V_c(t)]$ of the open-loop converter, by $X(t)$, then we write the system of equations governing the two states as

$$\frac{dX(t)}{dt} = A_1^o X(t) + B_1^o u \quad (1a)$$

$$V_{dc}(t) = C_1^o X(t) \quad (1b)$$

for $0 \leq t < T_1$ and

$$\frac{dX(t)}{dt} = A_2^o X(t) + B_2^o u \quad (2a)$$

$$V_{dc}(t) = C_2^o X(t) \quad (2b)$$

for $T_1 \leq t < T_2$, where

$$T = T_1 + T_2. \quad (3)$$

In (1) and (2), $V_{dc}(t)$ is the sum of $V_c(t)$ and the voltage drop across r_C . The matrices A_1^o , A_2^o , B_1^o , B_2^o , C_1^o , and C_2^o in (1) and (2) are given in Appendix I.

Using (1) and (2), we derive the open-loop state-space averaged model by taking the average of the states in the on- and off-intervals. This yields the following large-signal time-varying continuous system

$$\frac{d\overline{X}(t)}{dt} = (A_1^o d + A_2^o \overline{d}) \overline{X}(t) + (B_1^o d + B_2^o \overline{d}) \overline{u} \quad (4a)$$

$$\overline{V_{dc}}(t) = (C_1^o d + C_2^o \overline{d}) \overline{X}(t) \quad (4b)$$

where the duty ratio $d = T_1/T$.

Next we derive the exact solution of the open-loop system by stacking the consecutive solutions of (1) and (2) over

a switching period. The resulting discrete-time difference equation can be written in state-space form as

$$X_{k+1} = f_1^o(X_k, d_k, u) = \Phi(d_k)X_k + \Gamma(d_k)u \quad (5a)$$

$$V_{dc_{k+1}} = f_2^o(X_k, d_k, u) = C_2^o X_{k+1} \quad (5b)$$

where

$$\Phi(d_k) = \Phi_2(1 - d_k)\Phi_1(d_k), \quad \Phi_i(\tau) = e^{A_i^o \tau} \quad (6)$$

$$\begin{aligned} \Gamma(d_k) = & \Phi_2(1 - d_k) \int_0^{d_k T} \Phi_1(\tau) B_1^o d\tau \\ & + \int_0^{(1-d_k)T} \Phi_2(\tau) B_2^o d\tau. \end{aligned} \quad (7)$$

Using

$$\int_0^t e^{A_i^o \tau} B_i^o d\tau = [e^{A_i^o t} - I] (A_i^o)^{-1} B_i^o \quad (8)$$

and (6) and (7), we simplify the expression for X_{k+1} in (5a) to

$$\begin{aligned} X_{k+1} = & f_1^o(X_k, d_k, u) = e^{A_2^o(1-d_k)T} e^{A_1^o d_k T} X_k \\ & + e^{A_2^o(1-d_k)T} [e^{A_1^o d_k T} - I] (A_1^o)^{-1} B_1^o u \\ & + [e^{A_2^o(1-d_k)T} - I] (A_2^o)^{-1} B_2^o u. \end{aligned} \quad (9)$$

To derive a model for the closed-loop system, we assume that the m th-order, linear, time-invariant error amplifier (shown in Fig. 1) can be modeled as

$$\frac{d\xi(t)}{dt} = A_c \xi(t) + B_c u + B_{rc} V_{dcref} \quad (10a)$$

$$V_e(t) = H_c \xi(t) \quad (10b)$$

where

$\xi(t)$	$m \times 1$ state vector representing the states of the controller;
A_c	constant matrix;
B_c and B_{rc}	$m \times 1$ column vectors;
H_c	$1 \times m$ row vector;
V_{dcref}	reference voltage;
$V_e(t)$	output of the error amplifier.

Using (1), (2), and (10), we obtain the following equations for the closed-loop converter system

$$\frac{d\Psi(t)}{dt} = A_1 \Psi(t) + B_1 u + B_{r1} V_{dcref} \quad (11a)$$

$$V_{dc}(t) = C_1 \Psi(t) \quad (11b)$$

$$V_e(t) = P_1 \Psi(t) \quad (11c)$$

for $0 \leq t < T_1$ and

$$\frac{d\Psi(t)}{dt} = A_2 \Psi(t) + B_2 u + B_{r2} V_{dcref} \quad (12a)$$

$$V_{dc}(t) = C_2 \Psi(t) \quad (12b)$$

$$V_e(t) = P_2 \Psi(t) \quad (12c)$$

for $T_1 \leq t < T$. The matrices $A_1, A_2, B_1, B_2, B_{r1}, B_{r2}, C_1,$ and C_2 in (11) and (12) are given in Appendix II. Now $\Psi(t)$ represents the combined states of the controller and the power stage.

Using (11) and (12), we obtain the following state-space averaged model for the closed-loop system

$$\begin{aligned} \frac{d\bar{\Psi}(t)}{dt} = & [A_1 d + A_2 \bar{d}] \bar{\Psi}(t) + [B_1 d + B_2 \bar{d}] \bar{u} \\ & + [B_{r1} d + B_{r2} \bar{d}] V_{dcref} \end{aligned} \quad (13a)$$

$$\bar{V}_{dc}(t) = (C_1 d + C_2 \bar{d}) \bar{\Psi}(t). \quad (13b)$$

Similarly, we can write an exact discrete model for the closed-loop system in the form

$$\begin{aligned} \Psi_{k+1} = & f_1(\Psi_k, d_k, u) \\ = & e^{A_2(1-d_k)T} e^{A_1 d_k T} \Psi_k \\ & + [e^{A_2(1-d_k)T} (e^{A_1 d_k T} - I) (A_1)^{-1} B_1 \\ & + (e^{A_2(1-d_k)T} - I) (A_2)^{-1} B_2] u \\ & + [e^{A_2(1-d_k)T} (e^{A_1 d_k T} - I) (A_1)^{-1} B_{r1} \\ & + (e^{A_2(1-d_k)T} - I) (A_2)^{-1} B_{r2}] V_{dcref} \end{aligned} \quad (14a)$$

$$V_{dc_{k+1}} = f_2(\Psi_k, d_k, u) = C_2 \Psi_{k+1}. \quad (14b)$$

The auxiliary equation for the switching condition of the closed-loop feedback system is

$$\begin{aligned} \sigma(\Psi_k, d_k, u) = & \varphi \cdot [e^{A_1 d_k T} \Psi_k + (e^{A_1 d_k T} - I) (A_1)^{-1} \\ & \times (B_1 u + B_{r1} V_{dcref})] - V_{ramp} d_k \\ = & 0. \end{aligned} \quad (15)$$

In (15), the term φ represents the feedback controller and V_{ramp} is the magnitude of the ramp shown in Fig. 1. For example, for a lag-lead controller with an integrator

$$\varphi = \omega_m \begin{pmatrix} 0 & 0 & \omega_{z1} \omega_{z2} & (\omega_{z1} + \omega_{z2}) & 1 \end{pmatrix}.$$

The transfer function of the controller is

$$\begin{aligned} G_c(s) = & \frac{\omega_I (s + \omega_{z1})(s + \omega_{z2})}{s (s + \omega_{p1})(s + \omega_{p2})} \\ = & \frac{\omega_m \left(\frac{s}{\omega_{z1}} + 1 \right) \left(\frac{s}{\omega_{z2}} + 1 \right)}{s \left(\frac{s}{\omega_{p1}} + 1 \right) \left(\frac{s}{\omega_{p2}} + 1 \right)} \end{aligned} \quad (16)$$

where ω_I is the integrator gain and $\omega_{z1}, \omega_{z2}, \omega_{p1},$ and ω_{p2} are the zeros and poles of the controller.

For the filter shown in Fig. 1, the overall system analysis is done by augmenting the state-space representation of the voltage-mode converter with additional states of the filter, which forms its front stage. In this paper, we have chosen two second-order input filters having the following output impedance transfer function:

$$Z_{of}(s) = \frac{s^2(L_f C_f R_{f2}) + s(C_f R_{f1} R_{f2} + L_f) + R_{f1}}{s^2(L_f C_f) + s C_f (R_{f1} + R_{f2}) + 1}. \quad (17)$$

III. PERIOD-ONE RESPONSES AND THEIR STABILITY

The fixed points Ψ_k of (14) correspond to period-one limit cycles of the closed-loop regulator. They can be obtained by using the constraint $\Psi_{k+1} = \Psi_k = \Psi_s$. Letting $U = u$ and $D = d_k$

in (14), we find that the fixed points are given by (18), shown at the bottom of the page. Substituting (18) into (15), we obtain (19), shown at the bottom of the page. The transcendental equation (19) is solved numerically using a combination of the bisection and secant methods to determine the fixed points. To ascertain the stability of a given fixed point, we perturb the nominal values (Ψ_s, D, U, V_{dc_s}) as

$$\begin{aligned} \Psi &= \Psi_s + \hat{\Psi}, \quad d = D + \hat{d}, \quad u = U + \hat{u} \\ V_{dc} &= V_{dc_s} + \hat{V}_{dc}. \end{aligned} \quad (20)$$

Substituting (20) into (14) and (15), expanding the results in Taylor series, and keeping first-order terms, we obtain

$$\hat{\Psi}_{k+1} \approx \frac{\partial f_1}{\partial \Psi} \hat{\Psi}_k + \frac{\partial f_1}{\partial d} \hat{d}_k + \frac{\partial f_1}{\partial u} \hat{u} \quad (21)$$

$$\hat{V}_{dc_{k+1}} \approx \frac{\partial f_2}{\partial \Psi} \hat{\Psi}_k + \frac{\partial f_2}{\partial d} \hat{d}_k + \frac{\partial f_2}{\partial u} \hat{u} \quad (22)$$

$$0 \approx \frac{\partial \sigma}{\partial \Psi} \hat{\Psi}_k + \frac{\partial \sigma}{\partial d} \hat{d}_k + \frac{\partial \sigma}{\partial u} \hat{u}. \quad (23)$$

It follows from (23) that

$$\hat{d}_k = - \left[\frac{\partial \sigma}{\partial d} \right]^{-1} \left[\frac{\partial \sigma}{\partial \Psi} \hat{\Psi}_k + \frac{\partial \sigma}{\partial u} \hat{u} \right]. \quad (24)$$

Substituting (24) into (21) and (22) yields

$$\begin{aligned} \hat{\Psi}_{k+1} &\approx \left[\frac{\partial f_1}{\partial \Psi} - \frac{\partial f_1}{\partial d} \left(\frac{\partial \sigma}{\partial d} \right)^{-1} \frac{\partial \sigma}{\partial \Psi} \right] \hat{\Psi}_k \\ &\quad + \left[\frac{\partial f_1}{\partial u} - \frac{\partial f_1}{\partial d} \left(\frac{\partial \sigma}{\partial d} \right)^{-1} \frac{\partial \sigma}{\partial u} \right] \hat{u} \\ &= H_1 \hat{\Psi}_k + H_2 \hat{u} \end{aligned} \quad (25)$$

$$\begin{aligned} \hat{V}_{dc_{k+1}} &\approx \left[\frac{\partial f_2}{\partial \Psi} - \frac{\partial f_2}{\partial d} \left(\frac{\partial \sigma}{\partial d} \right)^{-1} \frac{\partial \sigma}{\partial \Psi} \right] \hat{\Psi}_k \\ &\quad + \left[\frac{\partial f_2}{\partial u} - \frac{\partial f_2}{\partial d} \left(\frac{\partial \sigma}{\partial d} \right)^{-1} \frac{\partial \sigma}{\partial u} \right] \hat{u} \\ &= H_3 \hat{\Psi}_k + H_4 \hat{u}. \end{aligned} \quad (26)$$

The stability of a given fixed point can be ascertained by the eigenvalues (Floquet multipliers) of H_1 [28], [29]. For asymptotic stability, all of the Floquet multipliers must be within the

unit circle. As a control parameter, such as the input voltage, is varied, we found that the fixed point loses stability by one of two scenarios. In the first scenario, a Floquet multiplier exits the unit circle in the complex plane through -1 . The post-instability response is a period-two limit cycle and the bifurcation is a flip or a period-doubling bifurcation [28], [29]. The bifurcation may be supercritical or subcritical, depending on whether the created period-two fixed point is stable or unstable. For supercritical bifurcations, the created period-two fixed point coexists with the unstable period-one fixed point. On the other hand, for subcritical bifurcations, the created period-two fixed point coexists with the stable period-one fixed point. In the second scenario, two complex conjugate Floquet multipliers exit the unit circle away from the real axis. The post-instability response is two-period quasiperiodic and the bifurcation is a Hopf bifurcation [28], [29]. The normal form of the Hopf bifurcation can be used to determine whether it is subcritical or supercritical. Alternatively, for supercritical bifurcations, the created quasiperiodic response coexists with the unstable period-one response; whereas for subcritical bifurcations, the created quasiperiodic response coexists with the stable period-one response.

IV. PERIOD-TWO FIXED POINTS AND THEIR STABILITY

To investigate the behavior of the period-doubled response, we construct a second-order map by imposing the constraint $\Psi_{k+2} = \Psi_k = \Psi_{2s}$. Using a methodology similar to that used in the period-one case, we construct the second-order map (27) and (28), shown at the bottom of the next page, where D_1, D_2, Ψ_{1s} , and Ψ_{2s} are the duty ratios and states corresponding to the period-two fixed points. The switching conditions are

$$\begin{aligned} \sigma_1(\Psi_{1s}, D_1, U) &= \varphi \cdot [e^{A_1 D_1 T} \Psi_{1s} + (e^{A_1 D_1 T} - I)(A_1)^{-1} \\ &\quad \times (B_1 U + B_{r1} V_{dcref})] - V_{ramp} D_1 = 0 \end{aligned} \quad (29)$$

$$\begin{aligned} \sigma_2(\Psi_{2s}, D_2, U) &= \varphi \cdot [e^{A_1 D_2 T} \Psi_{2s} + (e^{A_1 D_2 T} - I)(A_1)^{-1} \\ &\quad \times (B_1 U + B_{r1} V_{dcref})] - V_{ramp} D_2 = 0. \end{aligned} \quad (30)$$

The procedure for determining D_1, D_2, Ψ_{1s} , and Ψ_{2s} is the same as that used for the period-one fixed point except that we

$$\Psi_s = \left[I - e^{A_2(1-D)T} e^{A_1 D T} \right]^{-1} \left[\begin{array}{l} \left(e^{A_2(1-D)T} (e^{A_1 D T} - I)(A_1)^{-1} B_1 \right) U \\ + \left(e^{A_2(1-D)T} - I \right) (A_2)^{-1} B_2 \end{array} \right] U \\ + \left[\begin{array}{l} e^{A_2(1-D)T} (e^{A_1 D T} - I)(A_1)^{-1} B_{r1} \\ + \left(e^{A_2(1-D)T} - I \right) (A_2)^{-1} B_{r2} \end{array} \right] V_{dcref} \quad (18)$$

$$\sigma(\Psi_s, D, U) = \varphi \left[\begin{array}{l} e^{A_1 D T} \left(\begin{array}{l} \left(e^{A_2(1-D)T} (e^{A_1 D T} - I)(A_1)^{-1} B_1 \right) U \\ + \left(e^{A_2(1-D)T} - I \right) (A_2)^{-1} B_2 \end{array} \right) \\ + \left(e^{A_1 D T} - I \right) (A_1)^{-1} (B_1 U + B_{r1} V_{dcref}) \end{array} \right] - V_{ramp} D = 0. \quad (19)$$

need two initial guesses for the duty ratios. Guessing D_1 and D_2 , we determine Ψ_{1s} and Ψ_{2s} using (27) and (28) and then correct D_1 and D_2 using (29) and (30).

The stability of the period-two fixed points can be determined as before by perturbing them and forming the linearized variational equations

$$\hat{\Psi}_{k+2} = H_5 \hat{\Psi}_k + H_6 \hat{u} \quad (31)$$

$$\hat{V}_{dc_{k+2}} = H_7 \hat{\Psi}_k + H_8 \hat{u}. \quad (32)$$

Again the stability of the period-two orbit can be determined by calculating the Floquet multipliers of H_5 , which can be shown to be

$$H_5 = \begin{bmatrix} \frac{\partial f_1}{\partial \Psi_2} - \frac{\partial f_1}{\partial d_2} \left(\frac{\partial \sigma}{\partial d_2} \right)^{-1} \frac{\partial \sigma}{\partial \Psi_2} \\ \times \left[\frac{\partial f_1}{\partial \Psi_1} - \frac{\partial f_1}{\partial d_1} \left(\frac{\partial \sigma}{\partial d_1} \right)^{-1} \frac{\partial \sigma}{\partial \Psi_1} \right]. \end{bmatrix} \quad (33)$$

For stability, all of the Floquet multipliers of H_5 must be within the unit circle. So when the period-one orbit loses stability, the stability of the period-two orbit determines whether the period-doubling bifurcation is supercritical or subcritical. For the Hopf bifurcation, two complex conjugate multipliers leave the unit circle away from the real axis. The determination of whether the bifurcation is subcritical or supercritical can be done by calculating the normal form of the bifurcation. An alternate method is to find out whether there exists a periodic response with a period close to $(2\pi)/(\text{Im}(\lambda_{\text{Hopf}}))$ (where λ_{Hopf} is the complex multiplier exiting the unit circle) in the neighborhood of the bifurcation point as the bifurcation parameter is increased. If so then the Hopf bifurcation is supercritical. If not then, we can reduce the bifurcation parameter slowly and find out whether there are more than one stable solution by perturbing the period-one solution. If multiple stable solutions coexist, the Hopf bifurcation is subcritical. Of the multiple solutions one is the period-one solution. The others are global solutions.

V. STABILITY ANALYSIS USING THE LINEARIZED AVERAGED MODEL

For the averaged model, determination of the stability of the period-one solution can be done using the loop gain T_v of the voltage loop [30]. The loop gain of the closed-loop buck converter can be determined using

$$T_v(s) = G_d(s)G_c(s)(\text{FM})(f_s) \quad (34)$$

where

$$\begin{aligned} \text{FM} (=1/V_{\text{ramp}}) & \quad \text{modulator gain;} \\ f_s (=R_x/(R_x + R_y)) & \quad \text{feedback sensor gain;} \\ G_d(s) & \quad \text{control to the output transfer} \\ & \quad \text{function;} \end{aligned}$$

as shown in (35) at the bottom of the page, and $G_c(s)$ is the controller transfer function. The phase margin of T_v determines the stability of the closed-loop system.

For the filter, the overall system analysis is done by augmenting the state-space system of the voltage-mode converter with additional states of the filter, which forms its front stage. Analysis of the stability of the augmented system is the same as above once it is modeled with nonlinear maps. For the averaged model, we use the impedance criterion approach originally proposed by Middlebrook [31]. Stability, as per this criterion, demands that the input impedance (Z_{icl}) of the closed-loop converter be greater than the output impedance (Z_{of}) of the input filter. For the closed-loop converter, shown in Fig. 1, Z_{icl} can be shown to be

$$Z_{\text{icl}}(s) = \frac{[1 + T_v(s)]Z_{\text{icl}}(s)}{1 + T_v(s) - G_i(s)G_v(s)H(s)(\text{FM})(A)} \quad (36)$$

where $Z_{\text{icl}}(s)$, $G_i(s)$, and $G_v(s)$ represent the transfer functions for the open-loop input impedance, the control to the inductor current, and the audio susceptibility, respectively. They are given by (37)–(39), shown at the bottom of the next page. For some designs, if the strictly conservative condition for stability of the integrated system is violated, then an extended analysis

$$\Psi_{2s} = \left[I - e^{A_2(1-D_2)T} e^{A_1 D_2 T} e^{A_2(1-D_1)T} e^{A_1 D_1 T} \right]^{-1} \cdot \left[\begin{array}{l} \cdot (e^{A_2(1-D_1)T} (e^{A_1 D_2 T} - I) (A_1)^{-1} B_1 + (e^{A_2(1-D_1)T} - I) (A_2)^{-1} B_2) U \\ + (e^{A_2(1-D_1)T} (e^{A_1 D_2 T} - I) (A_1)^{-1} B_{r1} + (e^{A_2(1-D_1)T} - I) (A_2)^{-1} B_{r2}) V_{\text{dcref}} \\ + (e^{A_2(1-D_2)T} (e^{A_1 D_2 T} - I) (A_1)^{-1} B_1 + (e^{A_2(1-D_2)T} - I) (A_2)^{-1} B_2) U \\ + (e^{A_2(1-D_2)T} (e^{A_1 D_2 T} - I) (A_1)^{-1} B_{r1} + (e^{A_2(1-D_2)T} - I) (A_2)^{-1} B_{r2}) V_{\text{dcref}} \end{array} \right] \quad (27)$$

$$\begin{aligned} \Psi_{1s} &= e^{A_2(1-D_1)T} e^{A_1 D_1 T} \Psi_{2s} + \left(e^{A_2(1-D_1)T} (e^{A_1(1-D_1)T} - I) (A_1)^{-1} B_1 + (e^{A_2(1-D_1)T} - I) (A_2)^{-1} B_2 \right) U \\ &+ \left(e^{A_2(1-D_1)T} (e^{A_1(1-D_1)T} - I) (A_1)^{-1} B_{r1} + (e^{A_2(1-D_1)T} - I) (A_2)^{-1} B_{r2} \right) V_{\text{dcref}} \end{aligned} \quad (28)$$

$$G_d(s) = \left(\frac{R}{r_L + R} \right) u \frac{1 + sr_C C}{s^2 LC \left(\frac{R+r_C}{R+r_L} \right) + s \left(\frac{r_L R + r_L r_C + r_C R}{R+r_L} + \frac{L}{r_L + R} \right) + 1} \quad (35)$$

of the minor-loop gain $T_m (=Z_{of}/Z_{icl})$ using the Nyquist criterion needs to be done [31].

VI. EFFECT OF PARASITICS

In the above model, for the closed-loop system, the impact of device nonlinearities and parasitic dynamics was neglected. In conventional commercial converters, the switching frequency is equal to or greater than 100 kHz. At these high frequencies, the parasitics become very important and analysis based on nominal model may not be accurate. If the switching speed of the device (particularly the diode) is fast enough (for example using a Schottky diode), the impact of the device nonlinearity is reduced to some extent as long as the duty ratio of the system is not very small. However, the parasitic parameters vary from board to board, and hence, the parasitic dynamics are hard to control even with a well-designed PCB. To conduct the sensitive experiments reported in this paper, we had to design the board four times and make special arrangements to reduce the common-mode noise.

The impact of these very high-frequency dynamics (commonly called noise by practicing engineers) can be lumped into a stochastic recursion relation [32], [33]

$$\Psi_{k+1} = f_1(\Psi_k, d_k, u) + \Omega_k \chi. \quad (40)$$

The quantity Ω_k is a random variable controlled by an even distribution of unit width and χ is a variable that controls the width (or amplitude) of the noise. Equation (40) is identical to (14a) in the case of a deterministic quantity Ω_k .

This approach for studying the effect of external noise on the transition to chaos has been done in the past by physicists [32], [33]. However, the assumption of a Gaussian distribution is not always valid in power-electronic systems. This is because the distribution is skewed, primarily due to glitches in the power-converter response, and hence the mean and the median of the distribution are not the same. We consider a more direct approach here. We extract the parameters of the high-frequency model (based on the actual PCB layout) using the INCA software and high-speed design data books [34]. The INCA software is a finite-element analysis package and gives the self inductance associated with a trace and the mutual inductances associated with the coupling between traces [34]. We, however, neglect the mutual inductances because they are smaller than the self inductances by at least three orders of magnitude. As the switching frequency increases to the mega Hertz range, the

mutual inductance will become more prominent. Once the parameters have been extracted, we use the SABER software to simulate the higher-order system (Fig. 2). The snubber placed across the diode helps with very high-frequency ringing, with the response dynamics being faster than the switching frequency dynamics by three orders of magnitude. Therefore, we include the snubber in the high-frequency model. The power devices used in the simulation are actual models; they are used to account for the reverse recovery effect and junction capacitances associated with the devices.

VII. RESULTS

We present a bifurcation analysis of the closed-loop buck converter. We compare these results with those obtained by using the averaged model. Then, we present experimental results that we obtained with the buck converter shown in Fig. 3. We use an active load (in resistance mode) to study the influence of load resistance. Moreover, we present the theoretical and experimental results obtained for the integrated filter and converter. Then, we show the impact of the very high-frequency dynamics associated with parasitics and device nonlinearities on the onset of chaos. The system parameters for the closed-loop buck converter, second-order filters, and the high-frequency models are given in Appendix III. The converter we have chosen has a low output voltage and a wide variation in the input voltage. This is a typical scenario in a telecommunication application with a nominal input voltage of 48 V. As such the nominal duty ratio can be very low.

In Fig. 4, we present the frequency-response function obtained with the averaged model for the loop gain of a voltage-mode buck converter. The controller for the closed-loop system has the form $G_c(s) = (\omega_I/s)((s + \omega_{z1})(s + \omega_{z2})/((s + \omega_{p1})(s + \omega_{p2}))$. The worst phase margin is 20°, and hence the converter is stable according to the small-signal averaged model.

In Fig. 5, we show a bifurcation diagram for this closed-loop system. The load is kept at one ohm, and the input voltage, which is the bifurcation parameter, is varied between 20 to 62 V in increments of 0.1 V. The bifurcation diagram is constructed using the exact method and numerical techniques. The exact method works for u less than 55 V. Beyond that the system saturates and hence (15) is indeterminate. To carry on, we use numerical methods. The bifurcation analysis clearly shows a

$$Z_{iol}(s) = \left(\frac{r_L + R}{D^2} \right) \frac{s^2 LC \left(\frac{R+r_C}{R+r_L} \right) + s \left(\frac{r_L R + r_L r_C + r_C R}{R+r_L} + \frac{L}{r_L + R} \right) + 1}{1 + s r_C C} \quad (37)$$

$$G_v(s) = \frac{D(1 + s r_C C)}{s^2 LC + s \left(r_L C + r_C(1 - D)C + \frac{L}{r_C} \right) + 1} \quad (38)$$

$$G_i(s) = \left(\frac{Du}{r_L + R} \right) + D \left[\left(\frac{u}{r_L + R} \right) \frac{1 + s(r_C + R)C}{s^2 LC \left(\frac{R+r_C}{R+r_L} \right) + s \left(\frac{r_L R + r_L r_C + r_C R}{R+r_L} + \frac{L}{r_L + R} \right) + 1} \right]. \quad (39)$$

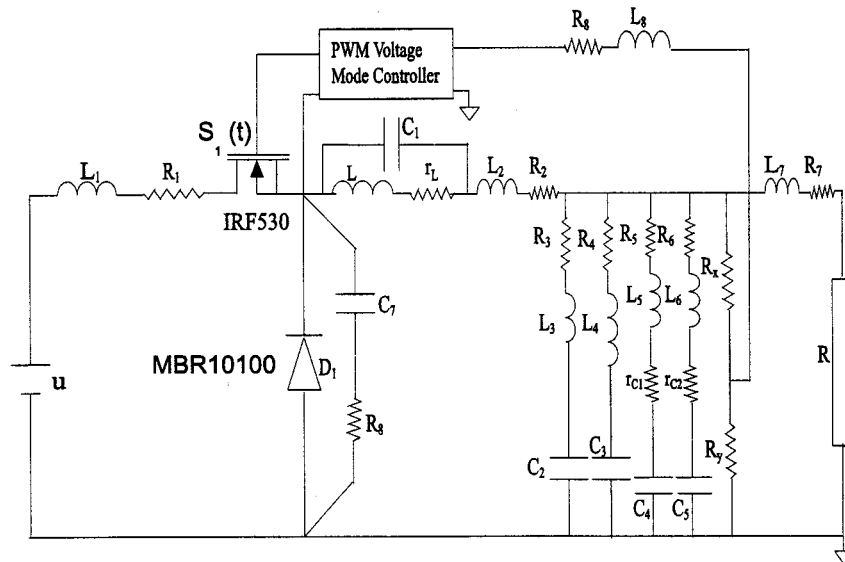


Fig. 2. High-frequency model of the closed-loop buck converter.

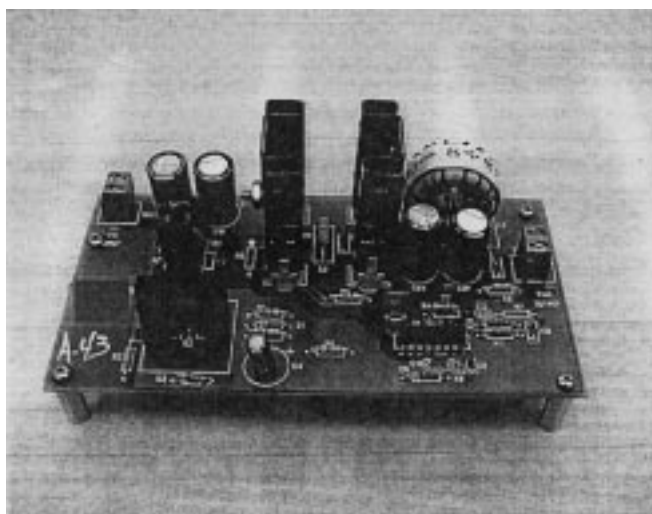


Fig. 3. Experimental closed-loop buck converter.

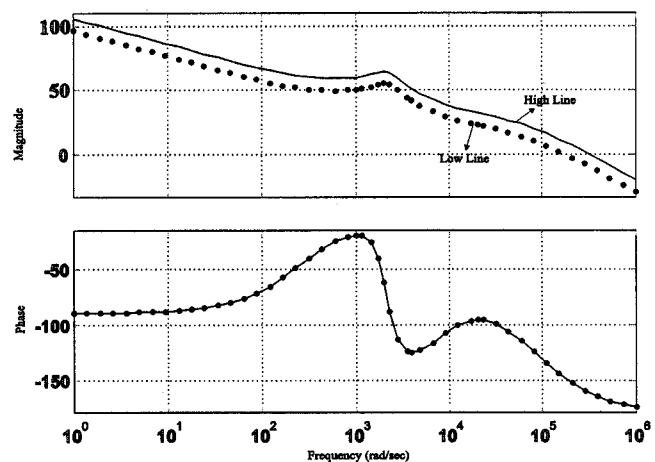


Fig. 4. Frequency-response analysis of the closed-loop buck converter. It shows a stable system.

fast-scale instability, which cannot be predicted with the state-space averaged model. Moreover, prediction of the period-one slow-scale instability with the linearized averaged model is conservative as compared to that obtained with the nonlinear averaged model.

It follows from Fig. 5 that the period-one orbits are stable for all values of the input voltage u below 53.8 V. All of the Floquet multipliers are within the unit circle. As u increases past 53.8 V, one of the Floquet multipliers exits the unit circle through -1 , as shown in Fig. 6, indicating a period-doubling or flip bifurcation. To study the stability of the created period-doubled orbits, we calculated the Floquet multipliers based on the second-order map for $u = 53.8$ V. The result is $[0.1288, 0.8302 + 0.0389i, 0.8302 - 0.0389i, 0.9039, 0.9911]$. Because all of these multipliers are inside the unit circle, the created period-two orbits are stable, and hence the period-doubling bifurcation is su-

percritical. Indeed, we were able to use long-time simulation to calculate period-two orbits beyond $u = 53.8$ V, as shown in the bifurcation diagram in Fig. 5.

Fig. 7(a) shows that the duty ratio undergoes a period-doubling bifurcation as u increases beyond 53.8 V. Immediately after the period-doubling bifurcation, all of the Floquet multipliers of the second-order map are within the unit circle: three of them are well within the unit circle and two are real and near $1 + 0i$, as shown in Fig. 7(b). In Fig. 7(c), we show the movement of the latter multipliers as u increases. They approach each other, collide, and move away from the real axis. It follows from Fig. 7(a) that as u approaches $u = u_c \approx 54.48$ V, one of the duty ratios approaches zero and at $u = u_c$ the error signal V_e hits the ramp at the bottom, as shown in Fig. 7(d). As such, the system saturates, which we have confirmed experimentally. This saturation or pulse dropping initiates the chaos, which is called

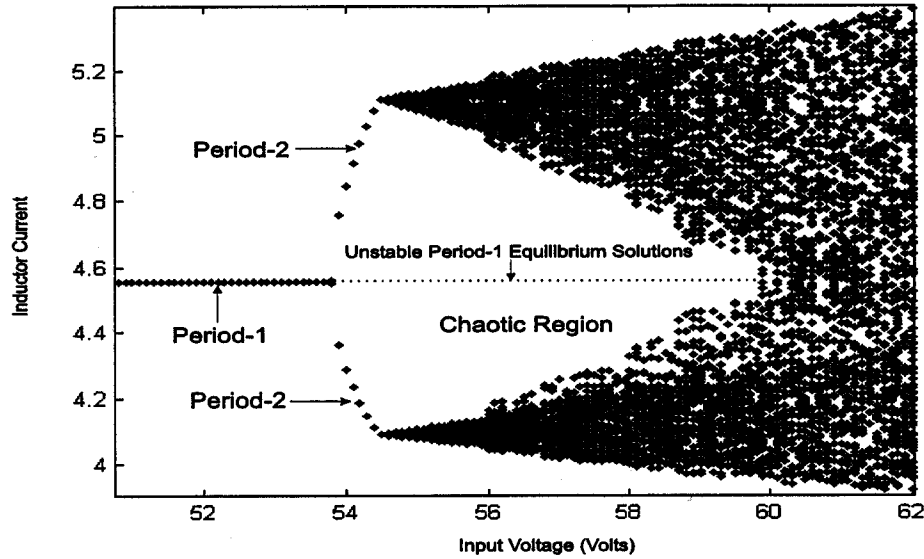


Fig. 5. Numerically obtained bifurcation diagram of the closed-loop buck converter. It shows a fast-scale instability.

border collision bifurcation by Nusse et al. [35] and Bannerjee et al. [21], [36]. Researchers in other fields have also reported similar nonsmooth bifurcations e.g., C-bifurcations in Filippov systems [37], [38] and grazing bifurcation in impacting systems [39]–[41]. In the saturated region, the second-order map used to derive (27) and (28) becomes invalid. As such, we are unable to plot the movement of the Floquet multipliers any more. For further increase in the input voltage, the response of the system becomes chaotic, which is shown in Fig. 5.

Once chaos is initiated, we resort to time-domain simulation using the switching model. In [42] the concept of impact map has been proposed. However, for the chaotic region, where the switching instant is unknown, the difference in the computation time between the simulation and the approach based on the impact map is negligible. It follows from the bifurcation diagram in Fig. 5 that initially chaos is confined to two small bands. As u is increased, the two chaotic bands increase in size until they collide with the unstable period-one response, resulting in a single large chaotic attractor in a so-called attractor-merging crisis [28].

We now explain, qualitatively, the transition in the response of the closed-loop converter from a period-two orbit to a chaotic attractor in the vicinity of $u = u_c$ by using Filippov's theory [10]. However, to proceed further, we use (11), (12) and Fig. 1, to describe the dynamics of the states of the closed-loop buck converter as a differential equation with discontinuous right-hand side; that is,

$$\begin{aligned} \frac{d\Psi(t)}{dt} &= A\Psi(t) + BS_1(t) + B_r V_{dcref} \\ S_1(t) &= \frac{1 + \text{sign}(V_e(t) - V_r(t))}{2} \\ &= \frac{1 + \text{sign}(V_e(t) - V_l - V_{ramp} \bmod(\frac{t}{T})f)}{2} \end{aligned} \quad (41)$$

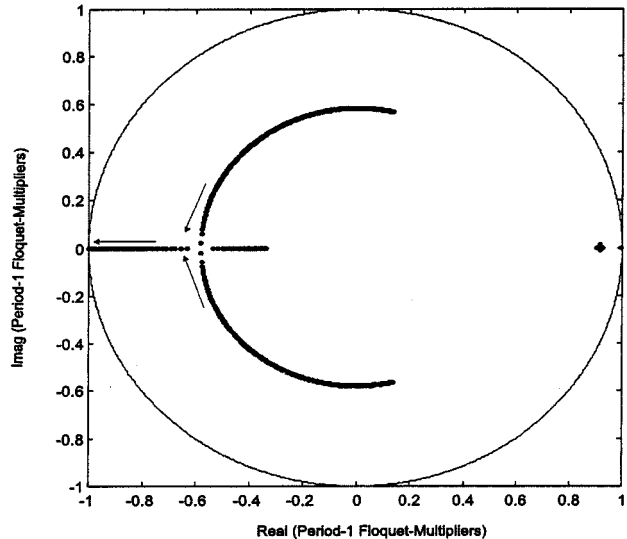


Fig. 6. One of the period-one Floquet multipliers exits the unit circle through -1 , indicating a period-doubling bifurcation.

where $f = 1/T$, $A = A_1 = A_2$, $B = B_1$, and $B_r = B_{r1} = B_{r2}$. Equation (41) shows that when $V_e(t) = V_r(t)$, then $d\Psi/dt$ is undefined. However, as long as $V_l < V_e(t) < V_l + V_{ramp}$ at the point of impact with the ramp, the latching action of our controller ensures only a single turn-on and a single turn-off of the power switch in a switching cycle. As such, one can describe the dynamics of the system using a nonlinear discrete map, thereby eliminating the discontinuity. One such map is used to obtain (27) and (28). The general form of this map is

$$\begin{aligned} \Psi_{k+2} &= (\Phi_4 \Phi_3 \Phi_2 \Phi_1) \Psi_k \\ &\quad + (\Phi_4 \Phi_3 \Phi_2 \Lambda_1 + \Phi_4 \Phi_3 \Lambda_2 + \Phi_4 \Lambda_3 + \Lambda_4) u \\ &\quad + (\Phi_4 \Phi_3 \Phi_2 \Upsilon_1 + \Phi_4 \Phi_3 \Upsilon_2 + \Phi_4 \Upsilon_3 + \Upsilon_4) V_{dcref} \end{aligned}$$

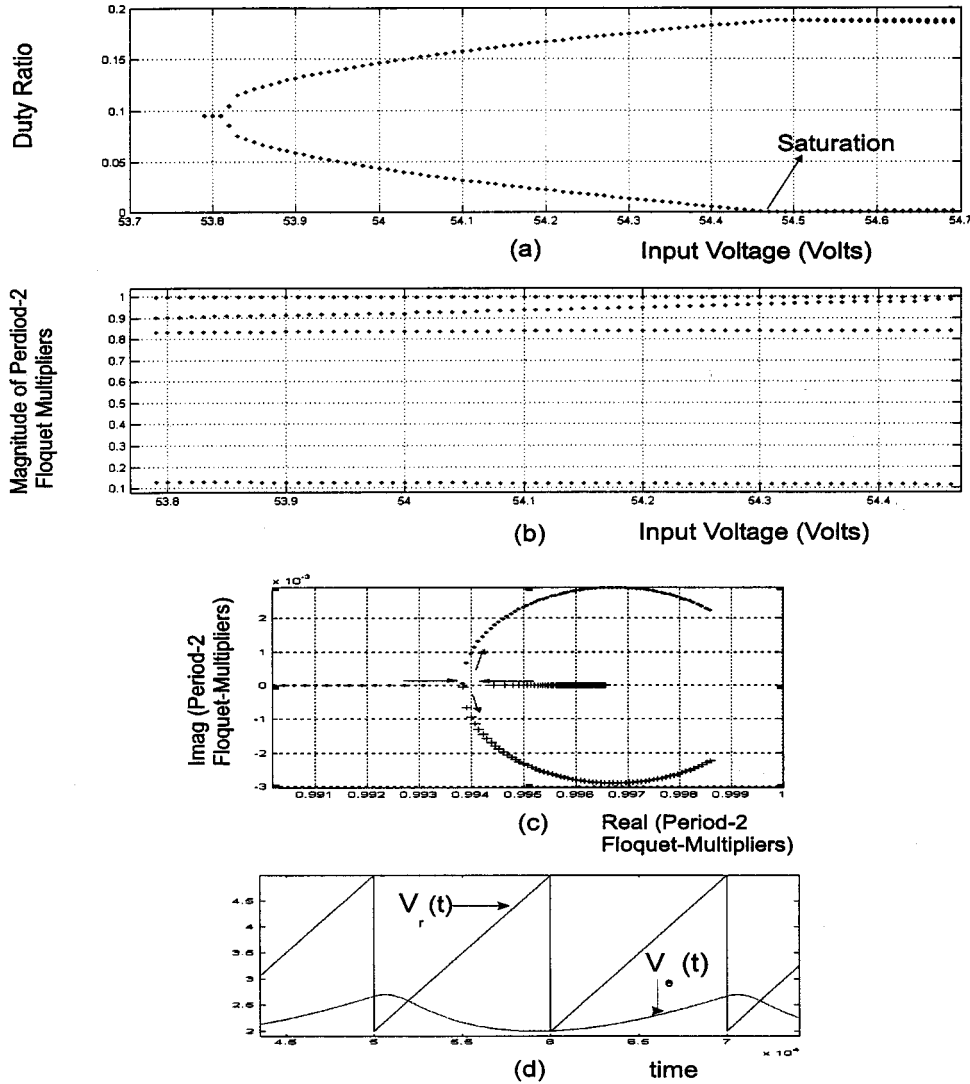


Fig. 7. (a) Variation of the duty ratio and (b) the magnitudes of the Floquet multipliers with the input voltage in the period-two region. (c) Two of the Floquet multipliers in (b) first collide with each other and then move toward the imaginary axis. (d) The error signal hits the ramp at the lowest point (at the beginning of the switching cycle) and the closed-loop system saturates.

$$\begin{aligned}
 V_{dc_{k+2}} &= P_1 \Psi_{k+2} \\
 0 &= \sigma_1(\Psi_k, d_{1k}, u) \\
 0 &= \sigma_2(\Psi_k, d_{1k}, d_{2k}, u)
 \end{aligned} \quad (42)$$

where Φ_s , Λ_s , Υ_s , and P_1 are matrices, and the last two scalar equations describe the switching conditions. When $V_e(t) = V_l$ (or $V_l + V_{\text{ramp}}$) at the point of impact with the ramp, (e.g., Fig. 7(d)), the system saturates and hence (42) fails. Using Fig. 7(d), we therefore construct another map as

$$\begin{aligned}
 \Psi_{k+2} &= (\underline{\Phi}_3 \underline{\Phi}_2 \underline{\Phi}_1) \Psi_k + (\underline{\Phi}_3 \underline{\Phi}_2 \underline{\Lambda}_1 + \underline{\Phi}_3 \underline{\Lambda}_2 + \underline{\Lambda}_3) u \\
 &\quad + (\underline{\Phi}_3 \underline{\Phi}_2 \underline{\Upsilon}_1 + \underline{\Phi}_3 \underline{\Upsilon}_2 + \underline{\Upsilon}_3) V_{\text{dcref}} \\
 V_{dc_{k+2}} &= P_2 \Psi_{k+2} \\
 0 &= \sigma_1(\Psi_k, d_{1k}, u)
 \end{aligned} \quad (43)$$

where $\underline{\Phi}_s$, $\underline{\Lambda}$, and $\underline{\Upsilon}$ are matrices. The nonlinear map (43) is valid at the point given by $V_e(t) = V_l$ and in the vicinity of

the fixed point. It is obvious that in the vicinity of saturation, the two maps (given by (42) and (43)) that describe the same system have different forms. Let J^- and J^+ be the Jacobian matrices that are obtained by linearizing (42) and (43) in the vicinity of the saturation point. Depending on the values of J^- and J^+ in the neighborhood of the saturation point, we can have two different sets of Floquet multipliers (FM^- and FM^+). In a smooth system, the transition from FM^- to FM^+ is always gradual. However, this is not the case in a nonsmooth system; it has many other other bifurcations than a smooth system [28]. The bifurcation diagram in Fig. 5 shows one such case, where chaos occurs due to saturation immediately after a period-doubling bifurcation. Although the Floquet multipliers are defined before and after the saturation point, they are not defined at this point. The Floquet multipliers at this point are obtained from the set-valued Jacobian matrix $J = [J^-, J^+]$. The viable solutions of this set are obtained by using the concept of convexity [10],

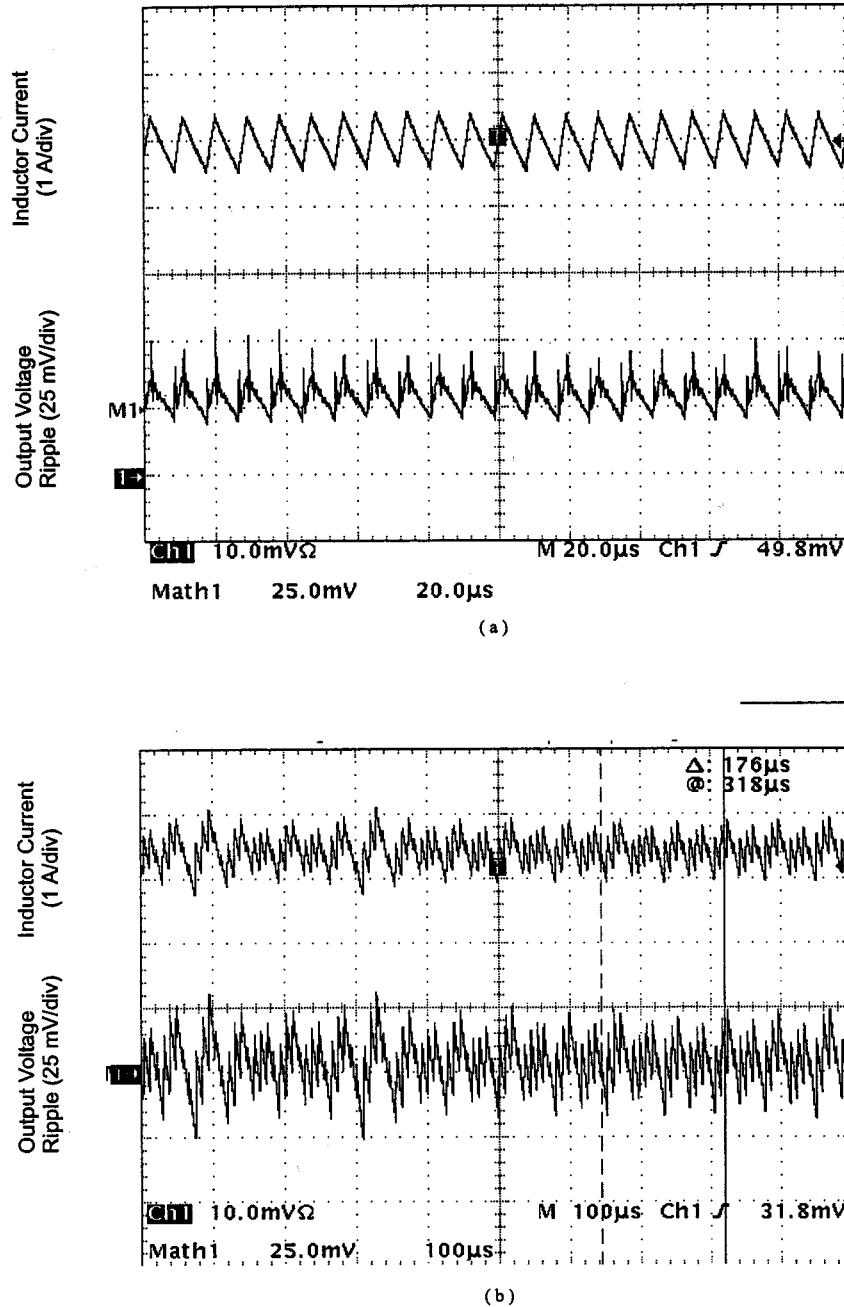


Fig. 8. Experimental waveforms for (a) period-one and (b) chaotic responses.

as shown in Appendix IV (for a differential equation with discontinuous right-hand side).

In Fig. 8, we show the experimental results we obtained for the converter in the stable and unstable regions with the input voltage as the bifurcation parameter. In Fig. 8(a), we show a stable period-one response. As u is increased to 52.6 V, the response becomes chaotic, as shown in Fig. 8(b), without undergoing a period-doubling bifurcation as predicted by the theory. To explain this discrepancy, we used the high-frequency model, shown in Fig. 2, to account for the impact of the very high-frequency dynamics due to parasitics and device nonlinearities.

The high-frequency model is developed using actual device models and parasitic parameters obtained using the actual PCB layout. The parasitic parameters are obtained from the PCB using the finite-analysis package INCA. In Fig. 9, we present the Fourier spectra of the bus voltage for two separate cases: one based on the high-frequency model and the other based on the nominal model, as shown in Fig. 1. These simulation results clearly indicate that the unmodeled uncertainties due to the very high-frequency dynamics cause the earlier onset of chaos.

Interestingly, the chaotic response is stable, and the ripple in the output voltage caused by chaos is tolerable, as seen from the

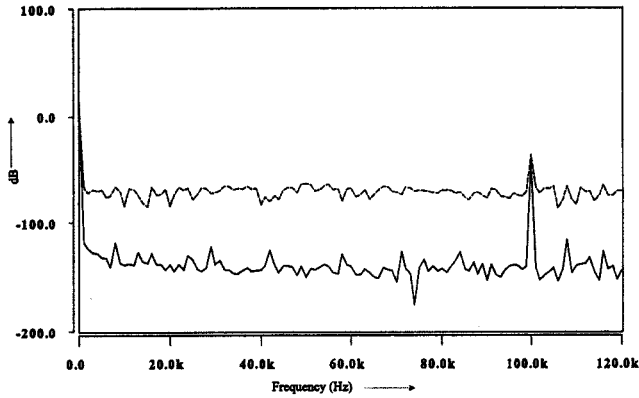


Fig. 9. Impact of parasitics on the onset of chaos. Fourier spectra of the output voltage based on the nominal model (bottom trace) and on the high-frequency model (top trace). The latter predicts an earlier onset of chaos.

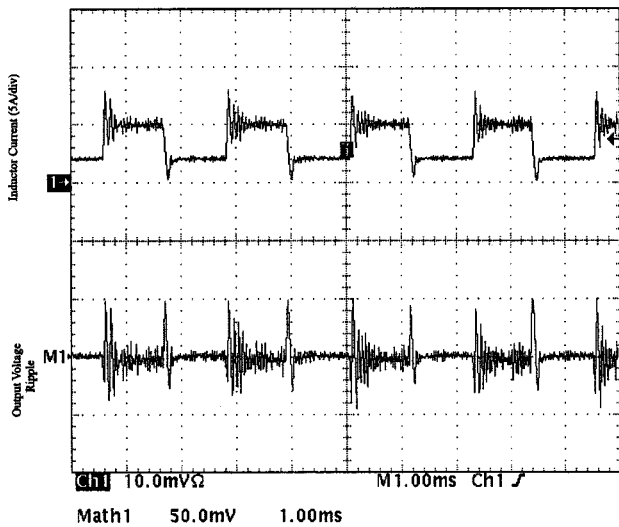


Fig. 10. Experimental result shows the influence of a transient-load change on the chaotic attractor.

experimental waveforms. We also performed a dynamic-load test when the converter is in the chaotic region, and the result is shown in Fig. 10. The load resistance was changed by 150% periodically every 1 ms. The test results show that chaos is stable. Within the chaotic region, we found narrow windows of periodic responses. Two such periodic waveforms are shown in Figs. 11(a) and (b).

Next, we demonstrate the slow-scale instability in the buck converter. The controller for the closed-loop systems has the form $G_c(s) = (\omega_I/s)(s + \omega_{z1})/(s + \omega_{p1})$. The frequency-response function for this case is shown in Fig. 12(a) for input voltages ranging from 20 to 62 V. The load resistance was kept constant at 5 Ω . For the nonlinear model, given the same system parameters, we found that two of the Floquet multipliers $[0.3119, 1.00001 + 0.0899i, 1.00001 - 0.0899i, 0.9533]$ exit the unit circle as complex conjugates at an input voltage of 31

V. Hence, both the averaged and discrete models predict the slow-scale instability.

The experimental result in Fig. 12(d) show that the response of the system suddenly bursts into an oscillation as the input voltage was gradually reduced below the point of instability. Beyond the point of instability, the current is not always in the CCM as seen from the theoretical and experimental results shown in Figs. 12(b) and (c). To analyze the dynamics beyond this point of instability, we had to switch between the CCM and DCM models. The CCM model was augmented with one more additional topology in which both the switch S_1 and diode D_1 are off. In other words, the system of (5) is modified as

$$\begin{aligned}
 X_{k+1} &= \Phi_3(t_3)\Phi_2(t_2)\Phi_1(t_1)X_k \\
 &+ \left[\Phi_3(t_3)\Phi_2(t_2) \int_0^{t_{11}} \Phi_1(\tau)B_1 d\tau \right. \\
 &+ \Phi_3(t_3) \int_{t_{11}}^{t_{12}} \Phi_2(\tau)B_2 d\tau \\
 &\left. + \int_{t_{12}}^T \Phi_3(\tau)B_3 d\tau \right] u_k \\
 V_{dc,k+1} &= C_3^o X_{k+1}
 \end{aligned} \tag{44}$$

where $\Phi_k(\tau) = e^{A_k^o \tau}$ [$k = 1, 3$] and $t_1 = t_{11} = d_k T, t_2 = t_{12} - t_{11}, t_3 = T - t_{12}$. The additional state-space matrices A_3^o, B_3^o , and C_3^o required for the DCM model are listed in Appendix II. In (4) the duty ratio is calculated as before. The additional timing information needed is the instant at which the inductor goes to zero in the discharging mode.

Next, we present the results obtained for an integrated system, which comprises the buck converter and a second-order filter at its front end. A complete bifurcation analysis for this case can be found in [23]. We consider two separate cases as before. The first is a stable integrated system based on the stability criterion of Middlebrook. The other is a poorly designed filter. The frequency-response plots of Z_{ic1} and Z_{of} for both cases are shown in Figs. 13(a) and (b). For the second case, in line with the result obtained for the standalone converter, we found that the slow-scale instability can be predicted by both the averaged and nonlinear models. Fig. 14(a) shows that when the input voltage is gradually reduced, the slow-scale instability occurs due to a Hopf bifurcation. Using the normal form of the large-signal averaged model in the vicinity of the bifurcation point, we found that the Hopf bifurcation is subcritical in nature. The averaged model, however, fails to predict the fast-scale instability in the first case, which is predicted by the nonlinear analysis and observed experimentally as shown in Fig. 14(b).

VIII. SUMMARY AND CONCLUSION

Using an exact formulation based on nonlinear maps, we investigate the fast-scale and slow-scale instabilities of a closed-loop converter and predicted the boundaries of these instabilities. For the standalone converter, the fast-scale instability results in a supercritical period-doubling bifurcation

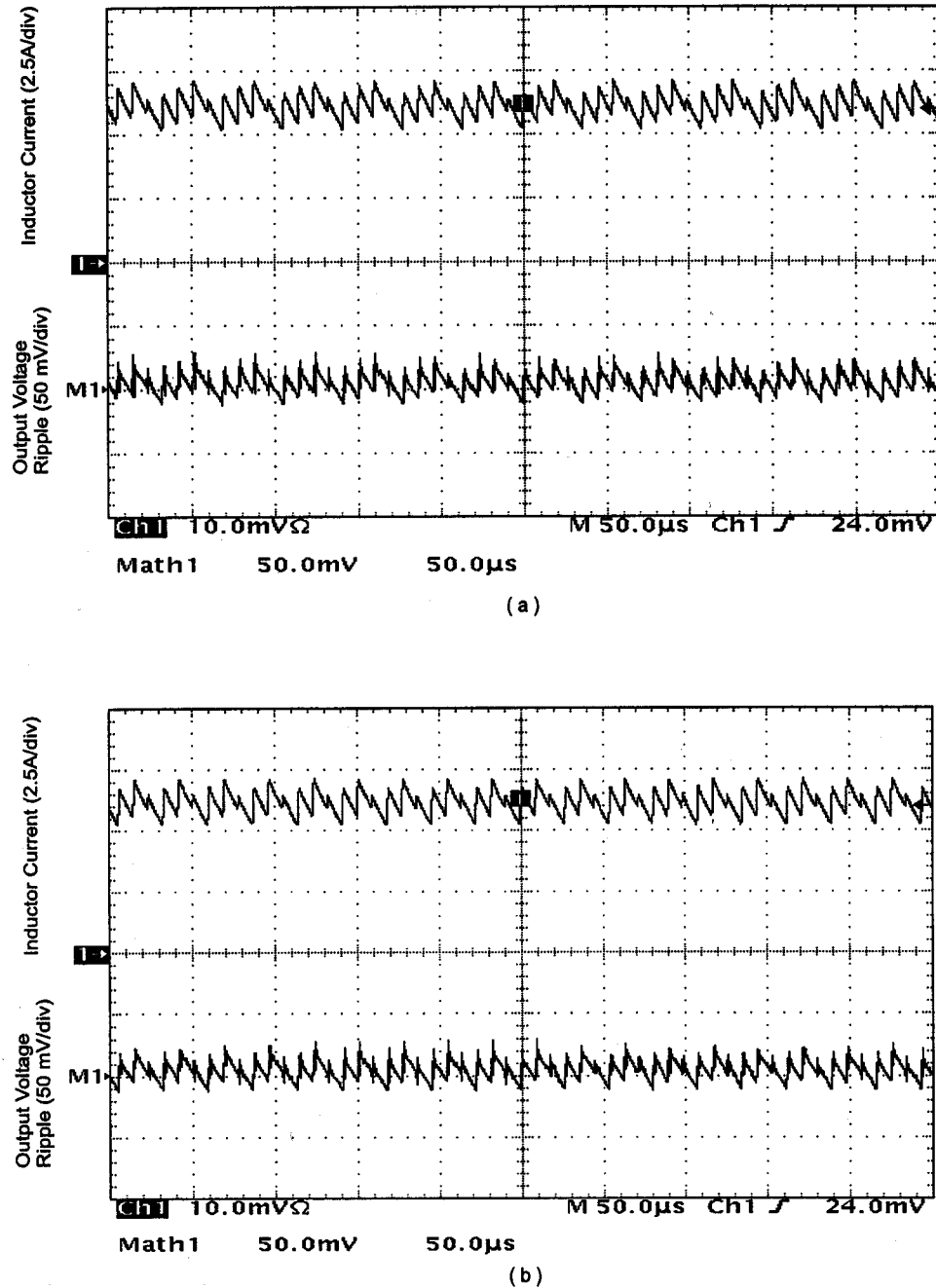


Fig. 11. Experimental result shows (a) period-4 and (b) period-3 waveform within the chaotic region.

followed by an intermittency of type-I route to chaos. The averaged model does not predict the boundary of the period-one instability correctly. Moreover, it can not account for post-instability dynamics.

We find similar results for an integrated system consisting of a second-order filter and a converter. We investigate two such integrated systems: one is stable as per Middlebrook's criterion [31] and the other is unstable. We find that this criterion fails to predict the fast-scale instability for the first design. For the second design, which is unstable on the slow scale, this criterion (which is based on linear analysis) does not give the domain of attrac-

tion of the period-one orbits near the bifurcation point. Using a nonlinear analysis [23], we find that the domain of attraction of the period-one orbits reduces considerably even before the Hopf bifurcation point due to the simultaneous presence of two stable and one unstable solutions. This reduces the disturbance rejection capability of the closed-loop system in this region. Conventional methods based on small-signal averaged-model techniques do not show this reduction in the domain of attraction.

The impact of parasitics on the onset of chaos is studied using a high-frequency model. The model is developed based on an actual PCB layout and power-device models. We find that the

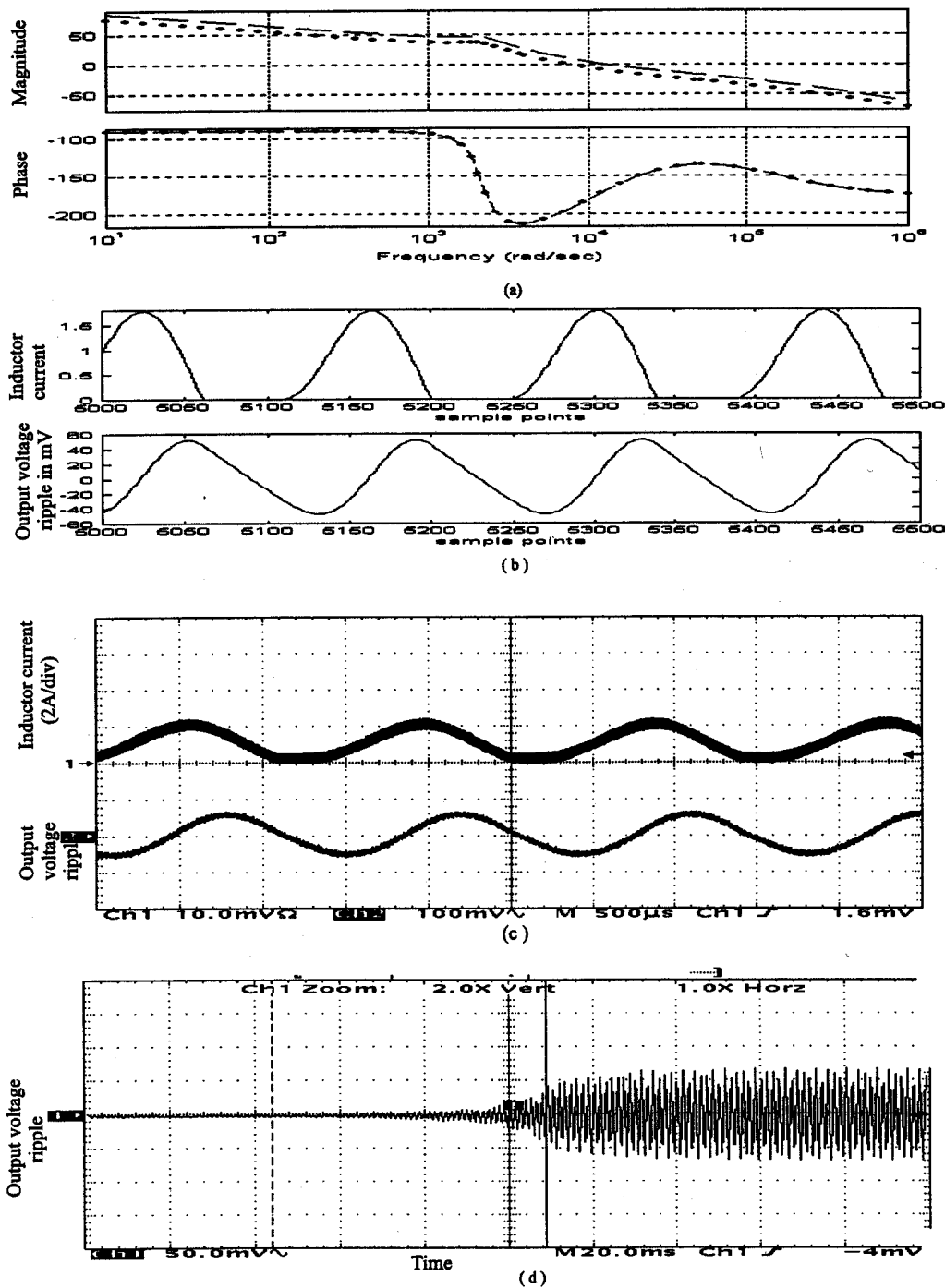


Fig. 12. Slow-scale instability of the closed-loop buck converter. (a) and (b) Linear and nonlinear analyses, which show an unstable response. (c) An experimental result that verifies the result in (b). (d) An experimental result that shows the onset of a sudden slow-scale instability as the input voltage (bifurcation parameter) is changed.

onset of chaos on the fast scale occurs earlier due to parasitics. However, it has negligible impact on the slow-scale instability. This is confirmed experimentally. The boundedness of the response in the chaotic region under transient-load conditions is confirmed experimentally.

The closed-loop converter system should be designed to operate away from the slow-scale instability boundary. However,

it can operate close to its fast-scale instability boundary. This will give the system a much higher bandwidth than that obtained using conventional designs. Thus by analyzing the nonlinear dynamics beyond the period-one region, one can improve the performance of the converter and correctly predict the boundaries of the instabilities. To extend the period-one operating regime, one can use bifurcation control.

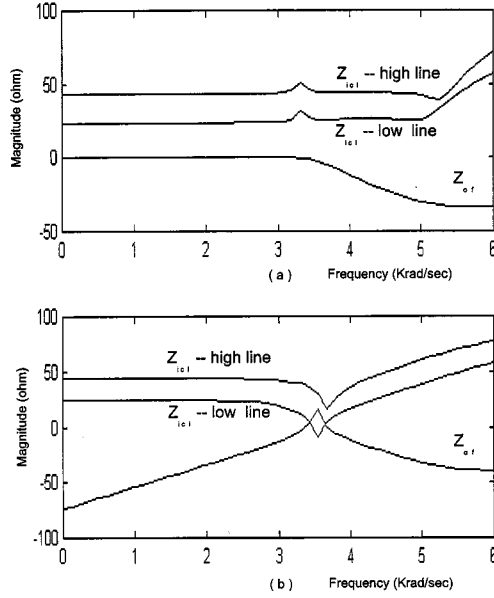


Fig. 13. Results of an integrated filter-converter system based on small-signal analysis. The frequency-response analyses based on Middlebrook's criterion predicts (a) stable and (b) unstable system.

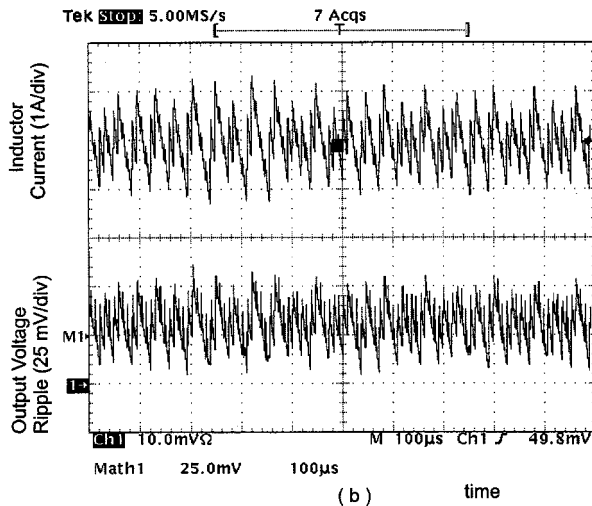
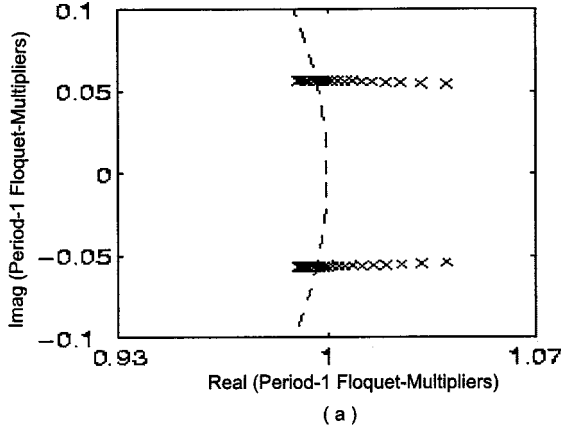


Fig. 14. (a) Nonlinear analysis shows a slow-scale instability for the second filter-converter system. (b) Experimental result that shows a fast-scale instability for the first filter-converter system.

APPENDIX I STATE-SPACE MATRICES FOR THE OPEN-LOOP BUCK CONVERTER

$$A_1^o = \begin{bmatrix} -\frac{r_L}{L} - \frac{r_C R}{(R+r_C)L} & -\frac{R}{(R+r_C)L} \\ \frac{R}{(R+r_C)C} & -\frac{1}{(R+r_C)C} \end{bmatrix}$$

$$B_1^o = \begin{bmatrix} \frac{1}{L} \\ 0 \end{bmatrix}, \quad C_1^o = \begin{bmatrix} \frac{r_C R}{R+r_C} & \frac{R}{R+r_C} \end{bmatrix}$$

$$A_2^o = \begin{bmatrix} -\frac{r_L}{L} - \frac{r_C R}{(R+r_C)L} & -\frac{R}{(R+r_C)L} \\ \frac{R}{(R+r_C)C} & -\frac{1}{(R+r_C)C} \end{bmatrix}$$

$$B_2^o = \begin{bmatrix} 0 \\ 0 \end{bmatrix}, \quad C_3^o = \begin{bmatrix} \frac{r_C R}{R+r_C} & \frac{R}{R+r_C} \end{bmatrix}$$

$$A_3^o = \begin{bmatrix} 0 & 0 \\ 0 & -\frac{1}{(R+r_C)C} \end{bmatrix}, \quad B_3^o = \begin{bmatrix} 0 \\ 0 \end{bmatrix}$$

$$C_3^o = \begin{bmatrix} \frac{r_C R}{R+r_C} & \frac{R}{R+r_C} \end{bmatrix} \quad (\text{for DCM only})$$

APPENDIX II STATE-SPACE MATRICES FOR THE CLOSED-LOOP BUCK CONVERTER

$$A_1 = \begin{bmatrix} A_1^o & 0 \\ SC_1^o & A_c \end{bmatrix}, \quad B_1 = \begin{bmatrix} B_1^o \\ 0 \end{bmatrix}, \quad B_{r1} = \begin{bmatrix} 0 \\ B_{rc} \end{bmatrix}$$

$$C_1 = [C_1^o \ 0], \quad H_1 = [H_c \ 0]$$

$$A_2 = \begin{bmatrix} A_2^o & 0 \\ f_s C_2^o & A_c \end{bmatrix}, \quad B_2 = \begin{bmatrix} B_2^o \\ 0 \end{bmatrix}, \quad B_{r2} = \begin{bmatrix} 0 \\ B_{rc} \end{bmatrix}$$

$$C_2 = [C_2^o \ 0], \quad H_2 = [H_c \ 0]$$

$$A_3 = \begin{bmatrix} A_3^o & 0 \\ f_s C_3^o & A_c \end{bmatrix}, \quad B_3 = \begin{bmatrix} B_3^o \\ 0 \end{bmatrix}, \quad B_{r3} = \begin{bmatrix} 0 \\ B_{rc} \end{bmatrix}$$

$$C_3 = [C_3^o \ 0], \quad H_3 = [H_c \ 0] \quad (\text{for DCM only})$$

where f_s is the feedback sensor gain.

APPENDIX III PARAMETERS OF THE CLOSED-LOOP SYSTEM

Nominal model parameters

$$L = 50 \mu\text{H}, \quad r_L = 21 \text{ m}\Omega, \quad r_C = 21 \text{ m}\Omega,$$

$$C_f = 4400 \mu\text{F}, \quad R = 1\Omega\text{--}5\Omega.$$

High-frequency model parameters

$$r_L = 21 \text{ m}\Omega, \quad r_C = 42 \text{ m}\Omega, \quad L = 50 \mu\text{H},$$

$$C_4 = 2200 \mu\text{F}, \quad C_5 = 2200 \mu\text{F}, \quad C_1 = 30 \text{ pF},$$

$$L_2 = 25 \text{ nH}, \quad R_2 = 150 \text{ m}\Omega, \quad L_3 = 5 \text{ nH},$$

$$R_3 = 25 \text{ m}\Omega, \quad C_2 = 100 \text{ nF}, \quad C_3 = 100 \text{ nF},$$

$$R_5 = 50 \text{ m}\Omega, \quad L_5 = 15 \text{ nH}.$$

Filter parameters

$$L_f = 200 \mu\text{H}, \quad R_{f1} = 100 \text{ m}\Omega, \quad R_{f2} = 21 \text{ m}\Omega,$$

$$C_f = 440 \mu\text{F}.$$

APPENDIX IV

FILIPPOV'S SOLUTION FOR A DISCONTINUOUS DIFFERENTIAL EQUATION

Let us consider the following vector differential equation:

$$\dot{y} = f(y, t, u(y)) = h(y, t) \quad (\text{A1})$$

where $h : \mathbb{R} \times \mathbb{R}^n \rightarrow \mathbb{R}^n$ is measurable and essentially locally bounded. A vector function $y(t)$, defined on the interval (t_1, t_2) , is a Filippov solution [10] of (A1) if it is absolutely continuous and, for almost all $t \in (t_1, t_2)$ and for arbitrary $\delta > 0$, the vector $dy(t)/dt$ belongs to the smallest convex closed set of an n -dimensional space containing all of the values of the vector function $h(t, y')$; where y' ranges over the entire δ neighborhood of the point $y(t)$ in the space y (with t fixed) except for a set of measure $\mu N = 0$; that is

$$\frac{dy(t)}{dt} \in K[h](y, t) \quad (\text{A2})$$

where $K[h](\cdot)$ is called the Filippov's differential inclusion and is defined as

$$K[h](t, y) \equiv \bigcap_{\delta > 0} \bigcap_{\mu N > 0} \overline{\text{co}} h(B(y, \delta) - N). \quad (\text{A3})$$

In differential inclusion (A2), $\overline{\text{co}}$ denotes the convex hull of a set, N represents a set of zero Lebesgue measure, μN and B is a ball of radius δ centered at y . The content of Filippov's solution is that the tangent vector to a solution at a time t , where it exists, must lie in the convex closure of the limiting values of the vector field in progressively smaller neighborhoods around the solution evaluated at time t .

Let us now consider a single switching surface H , which is a smooth surface (manifold) separating the space into regions H^+ and H^- . Suppose that H is regular so that it can be divided by a smooth real-valued function $\sigma(y)$ (i.e., $H = \{y : \sigma(y) = 0 = 0\}$) and suppose that $h(t, y)$ is bounded and, for any fixed t , its limiting values $h^+(y, t)$ and $h^-(y, t)$ exist when H is approached from H^+ and H^- . Let $h_0^+(y, t)$ and $h_0^-(y, t)$ be the projections of $h^+(y, t)$ and $h^-(y, t)$ on the normal $\nabla\sigma$ to the surface H directed toward H^+ and H^- . Then, for an absolutely continuous $y \in H$ satisfying $h_0^+(y, t) \leq 0$, $h_0^-(y, t) \geq 0$, and $h_0^-(y, t) - h_0^+(y, t) > 0$, the trajectories pointing toward H are solutions of (A1) according to the differential inclusion (A2) if and only if

$$\frac{dy}{dt} = \beta(t)h^+(y, t) + (1 - \beta(t))h^-(y, t) \quad (\text{A4})$$

where

$$\beta(t) = \frac{h_0^-(y, t)}{h_0^-(y, t) - h_0^+(y, t)}. \quad (\text{A5})$$

We note that the right-hand side of (A4) is orthogonal to $\nabla\sigma$ and hence the solution remains on the surface H .

ACKNOWLEDGMENT

The authors would like to thank E. Walker and M. Dennis, Texas Instruments, for their help during the course of experimentation.

REFERENCES

- [1] R. D. Middlebrook and S. Cuk, "A general unified approach to modeling switching-converter power stages," in *Proc. IEEE Power Electron. Spec. Conf.*, 1977, pp. 521–550.
- [2] —, "A general unified approach to modeling switching dc to dc converters in discontinuous conduction mode," in *Proc. IEEE Power Electron. Spec. Conf.*, 1977, pp. 36–57.
- [3] V. Vorperian, "Simplified analysis of pwm converters using model of pwm switch. Continuous conduction mode," *IEEE Trans. Aerosp. Electron. Syst.*, vol. 26, pp. 490–496, May 1990.
- [4] —, "Simplified analysis of pwm converters using model of pwm switch. II. Discontinuous conduction mode," *IEEE Trans. Aerosp. Electron. Syst.*, vol. 26, pp. 497–505, May 1990.
- [5] A. R. Brown and R. D. Middlebrook, "Sampled-data modeling of switching regulators," in *Proc. IEEE Power Electron. Spec. Conf.*, 1981, pp. 346–369.
- [6] R. B. Ridley, "A new continuous-time model for current-mode control," *IEEE Trans. Power Electron.*, vol. 6, pp. 271–280, Mar. 1991.
- [7] D. J. Short and F. C. Lee, "An improved switching converter model using discrete and averaging techniques," *IEEE Trans. Aerosp. Electron. Syst.*, vol. AES-19, pp. 190–202, Feb. 1983.
- [8] G. C. Verghese, M. E. Elbuluk, and J. G. Kassakian, "A general approach to sampled-data modeling for power electronic circuits," *IEEE Trans. Power Electron.*, vol. PEL-1, pp. 76–89, Mar. 1986.
- [9] V. I. Utkin, *Sliding Modes in Control Optimization*. New York: Springer-Verlag, 1992.
- [10] A. F. Filippov, *Differential Equations with Discontinuous Righthand Sides*. Amsterdam, The Netherlands: Kluwer, 1988.
- [11] J. Aubin and A. Cellina, *Differential Inclusions: Set-Valued Maps and Viability Theory*. New York: Springer-Verlag, 1984.
- [12] S. K. Mazumder, A. H. Nayfeh, and D. Borojević, "Development of integral-variable-structure control schemes for parallel-buck and parallel-boost dc-dc converters," in *Proc. IEEE Int. Telecommun. Energy Conf.*, 2000.
- [13] —, "A new approach to the stability analysis of boost power-factor-correction circuits," in *Proc. Annual Sem. Ctr. Power Electron. Syst.*, 2000.
- [14] R. Prajoux, J. C. Marpinard, and J. Jalade, "Etablissement de modeles mathematiques pour regulateurs de puissance a modulation de largeur d'impulsions (pwm)," *ESA Sci. Tech. Rev.*, vol. 2, pp. 25–42, 1976.
- [15] J. R. Wood, "Chaos: A real phenomenon in power electronics," in *Proc. IEEE Appl. Power Electron. Conf. Expo.*, 1989, pp. 115–124.
- [16] J. H. B. Deane and D. C. Hamill, "Analysis, simulation and experimental study of chaos in the buck converter," in *Proc. IEEE Power Electron. Spec. Conf.*, 1990, pp. 491–498.
- [17] D. C. Hamill and J. H. B. Deane, "Modeling of chaotic dc-dc converters by iterated nonlinear mappings," *IEEE Trans. Power Electron.*, vol. 7, pp. 25–36, Jan. 1992.
- [18] E. Fossas and G. Olivar, "Study of chaos in the buck converter," *IEEE Trans. Circuits Syst. I*, vol. 43, pp. 13–25, Jan. 1996.
- [19] C. K. Tse and K. M. Adams, "Qualitative analysis and control of a dc-to-dc boost converter operating in discontinuous mode," *IEEE Trans. Power Electron.*, vol. 5, pp. 323–330, May 1990.
- [20] C. K. Tse, "Flip bifurcation and chaos in three-state boost switching regulators," *IEEE Trans. Circuits Syst. I*, vol. 41, pp. 16–23, Jan. 1994.
- [21] S. Banerjee, E. Ott, J. A. Yorke, and G. H. Yuan, "Anomalous bifurcations in dc-dc converters: Borderline collisions in piecewise smooth maps," in *Proc. IEEE Power Electron. Spec. Conf.*, 1997, pp. 1337–1344.
- [22] I. Zafrany and B. Yaakov, "A chaos model of subharmonic oscillations in current mode PWM boost converters," in *Proc. IEEE Power Electron. Spec. Conf.*, 1995, pp. 1111–1117.
- [23] M. Alfayoumi, A. H. Nayfeh, and D. Borojević, "Input filter interactions in dc-dc switching regulators," in *Proc. IEEE Power Electron. Spec. Conf.*, 1999, pp. 926–932.
- [24] S. K. Mazumder, M. Alfayoumi, A. H. Nayfeh, and D. Borojević, "A theoretical and experimental investigation of the nonlinear dynamics of dc-dc converters," in *Proc. IEEE Power Electron. Spec. Conf.*, 2000, pp. 729–734.

- [25] M. Alfayoumi, A. H. Nayfeh, and D. Borojević, "Modeling and analysis of switching-mode dc-dc regulators," *Int. J. Bifurc. Chaos*, submitted for publication.
- [26] S. K. Mazumder, A. H. Nayfeh, and D. Borojević, "Nonlinear dynamics and stability analysis of parallel dc-dc converters," in *Proc. Annu. Sem. Ctr. Power Electron. Syst.*, 2000.
- [27] D. C. Hamill, "Power electronics: A field rich in nonlinear dynamics," in *Proc. 3rd Int. Specialists' Workshop Nonlinear Dyn. Electron. Syst.*, 1995, pp. 165-178.
- [28] A. H. Nayfeh and B. Balachandran, *Applied Nonlinear Dynamics*. New York: Wiley, 1995.
- [29] D. M. Wolf, M. Verghese, and S. R. Sanders, "Bifurcation of power electronic circuits," *J. Franklin Inst.*, pp. 957-999, 1994.
- [30] F. C. Lee, *Modeling, Analysis, and Design of PWM Converter*. Blacksburg, VA: Virginia Power Electronics Center, 1990.
- [31] R. D. Middlebrook, "Input filter considerations in design and application of switching regulators," *Proc. IEEE Ind. Applicat.*, pp. 91-107, Oct. 1976.
- [32] J. Crutchfield, M. Nauenberg, and J. Rudnick, "Scaling for external noise at the onset of chaos," *Phys. Rev. Lett.*, vol. 46, no. 14, pp. 933-939, 1981.
- [33] J. Crutchfield and B. A. Huberman, "Fluctuations and the onset of chaos," *Phys. Lett.*, vol. 77A, no. 6, pp. 407-410, 1980.
- [34] W. Zhang, "Integrated EMI/Thermal Design for Switching Power Supplies," M.S. thesis, Dept. Elect. Eng., Virginia Polytech. Inst. & State Univ., Blacksburg, 1998.
- [35] H. E. Nusse and J. A. York, "Border-collision bifurcations including period two to period three for piecewise smooth systems," *Phys. D*, vol. 57, pp. 39-57, 1992.
- [36] S. Banerjee and C. Grebogi, "Border collision bifurcations in two dimensional piecewise smooth maps," *Phys. Rev. E*, vol. 59, no. 4, pp. 4052-4061, 1999.
- [37] M. I. Feigin, "On the structure of C-bifurcation boundaries of piecewise-continuous systems," *PMM*, vol. 38, no. 5, pp. 810-818, 1974.
- [38] —, "The increasingly complex structure of the bifurcation tree of a piecewise-smooth system," *J. Appl. Math Mech.*, vol. 59, no. 6, pp. 853-863, 1995.
- [39] A. P. Ivanov, "Analytical methods in the theory of vibro-impact systems," *J. Appl. Math Mech.*, vol. 57, no. 3, pp. 221-236, 1993.
- [40] A. B. Nordmark, "Universal limit mapping in grazing bifurcations," *Phys. Rev.*, vol. 55, no. 1, pp. 266-270, 1997.
- [41] B. Brogliato, *Nonsmooth Mechanics*, London, U.K.: Springer, 1999.
- [42] M. D. Bernardo, F. Garofalo, and F. Vasca, "Switchings, bifurcations, and chaos in dc/dc converters," *IEEE Trans. Circuits Syst. I*, vol. 45, pp. 133-141, Feb. 1998.



Sudip K. Mazumder received the M.S. degree in electrical power engineering from the Rensselaer Polytechnic Institute, Troy, NY, in 1993 and is currently pursuing the Ph.D. degree in electrical and computer engineering at the Center for Power Electronics Systems (CPES), Virginia Polytechnic Institute and State University, Blacksburg.

He has eight years of professional experience in the area of power electronics, motion drives, and motion control. His areas of interest include nonlinear analysis and control of standalone, integrated, and parallel

dc-dc and multiphase power converters, hybrid systems, DSP/RISC-based high-performance standalone and multi-axis drives and multiphase converters, electric/hybrid vehicles, multilevel converters for applications in power systems and high power drives, active filters, integration of power converters, soft- and hard-switching topologies, and techniques in power converters. Currently, he has eighteen international journals and conference papers, and is the reviewer for five international journals.

Dr. Mazumder has been selected as Session Chair on "Motor Drives" for the IEEE Power Electronics Specialists Conference, 2001.



Ali H. Nayfeh received the B.S. degree in engineering science and the M.S. and Ph.D. degrees in aeronautics and astronautics, all from Stanford University, Stanford, CA, in 1962, 1963, and 1964, respectively.

He is a University Distinguished Professor of Engineering in the Department of Engineering Science and Mechanics, Virginia Polytechnic Institute and State University, Blacksburg. He is internationally well known for his work in perturbation methods, nonlinear analysis, nonlinear dynamics, structural

dynamics, fluid-structure-control interactions, and nonlinear active control of dynamical systems. He is the author or co-author of seven books by Wiley and three books by Dynamic Press. A number of these books are translated into Russian and Chinese and adopted in classes at universities worldwide. He is the Editor-in-Chief of the journal *Nonlinear Dynamics* and the *Journal of Vibration and Control*. He is also the Editor of the Wiley Book Series on Nonlinear Science. He published 350 articles in referred journals and 35 book chapters, made 434 presentations at national and international meetings, and gave 103 seminars at universities worldwide. He has advised 56 Ph.D. Dissertations.

Dr. Nayfeh received the ASME Den Hartog Award, in recognition of lifetime contributions to the teaching and practice of vibration engineering, and the AIAA Pendray Aerospace Literature Award, for seminal contributions to perturbation methods, nonlinear dynamics, acoustics, and boundary-layer theory; praiseworthy for their quality, relevance, timeliness, and lasting influence on the aerospace community. He holds two Honorary Doctorates, one from the Marine Technical University, St. Petersburg, Russia, and the other from the Technical University of Munich, Germany. He is a Fellow of the American Academy of Mechanics, the American Society of Mechanical Engineering (ASME), The American Institute of Aeronautics and Astronautics (AIAA), and the American Physical Society. He is the Director of the Multidisciplinary University Research Initiative on Nonlinear Active Control of Dynamical Systems and a Defense University Infrastructure Program to build a Physics-Based Ship- and Crane Simulator in the CAVE, both sponsored by ONR.



Dushan Borojević (M'85) received the B.S. degree from the University of Belgrade, Yugoslavia, in 1976, the M.S. degree from the University of Novi Sad, Yugoslavia, in 1982, and the Ph.D. degree from the Virginia Polytechnic Institute and State University (Virginia Tech), Blacksburg, in 1986.

Between 1986 and 1990, he was an Assistant Professor and Director of the Power and Industrial Electronics Research Program, Institute for Power and Electronic Engineering, University of Novi Sad. In 1990, he joined The Bradley Department of

Electrical and Computer Engineering, Virginia Tech, as Associate Professor. From 1996 to 1998, he was Associate Director of the Virginia Power Electronics Center, and since 1998 he has been the Deputy Director of the NSF Engineering Research Center for Power Electronics Systems, where he is now a Full Professor. His research interests include multiphase power conversion, high-power PWM converters, modeling and control of power converters, applied digital control, and electrical drives. He has published over 100 technical papers, has three patents, and has been involved in numerous government and industry-sponsored projects in the areas of power and industrial electronics.

Dr. Borojević is a member of the IEEE Power Electronics Society AdCom, the IEEE Industry Applications Society Industrial Power Converter Committees, and Phi Kappa Phi.